Monthly Notices
of the
ROYAL ASTRONOMICAL SOCIETY

Mon. Not. R. Astron. Soc. **421,** 356–368 (2012) doi:10.1111/j.1365-2966.2011.20310.x

Origin and detectability of co-orbital planets from radial velocity data

C. A. Giuppone,[1,2]★ P. Benítez-Llambay[1,3] and C. Beaugé[1,3]

[1]*Observatorio Astronómico, Universidad Nacional de Córdoba, Laprida 854, X5000BGR Córdoba, Argentina*
[2]*Departamento de Física, I3N, Universidade de Aveiro, Campus de Santiago, 3810-193 Aveiro, Portugal*
[3]*Instituto de Astronomía Teórica y Experimental, Laprida 854, X5000BGR Córdoba, Argentina*

Accepted 2011 December 1. Received 2011 November 29; in original form 2011 October 4

ABSTRACT

We analyse the possibilities of detection of hypothetical exoplanets in co-orbital motion from synthetic radial velocity (RV) signals, taking into account different types of stable planar configurations, orbital eccentricities and mass ratios. For each nominal solution corresponding to small-amplitude oscillations around the periodic solution, we generate a series of synthetic RV curves mimicking the stellar motion around the barycentre of the system. We then fit the data sets obtained assuming three possible different orbital architectures: (a) two planets in co-orbital motion, (b) two planets in a 2/1 mean-motion resonance (MMR) and (c) a single planet. We compare the resulting residuals and the estimated orbital parameters.

For synthetic data sets covering only a few orbital periods, we find that the discrete RV signal generated by a co-orbital configuration could be easily confused with other configurations/systems, and in many cases the best orbital fit corresponds to either a single planet or two bodies in a 2/1 resonance. However, most of the incorrect identifications are associated with dynamically unstable solutions.

We also compare the orbital parameters obtained with two different fitting strategies: a simultaneous fit of two planets and a nested multi-Keplerian model. We find that, even for data sets covering over 10 orbital periods, the nested models can yield incorrect orbital configurations (sometimes close to fictitious MMRs) that are nevertheless dynamically stable and with orbital eccentricities lower than the correct nominal solutions.

Finally, we discuss plausible mechanisms for the formation of co-orbital configurations, by the interaction between two giant planets and an inner cavity in the gas disc. For equal-mass planets, both Lagrangian and anti-Lagrangian configurations can be obtained from same initial condition depending on final time of integration.

Key words: techniques: radial velocities – celestial mechanics – planets and satellites: formation.

1 INTRODUCTION

The possible existence of exoplanets in co-orbital motion has fascinated planetary scientists for several years. Since the diversity of exoplanetary configurations continues to surprise us, even more than 15 years after the discovery of Peg51b, it seems almost natural to expect Trojan planets to exist somewhere and the announcement of their discovery to be only a matter of time. Probably the first detailed analysis of hypothetical co-orbital planets is due to Laughlin & Chambers (2002). They studied three types of co-orbital configurations: tadpole orbits (around L_4 and L_5 equilateral points), horse-shoe configurations and 'eccentric resonances'. They proposed to distinguish between co-orbital and single-planet fits from radial velocity (RV) data by observing residuals from long-term observations (more than 10 orbital periods), because the co-orbital configurations have large mutual interactions due to resonant motion.

For systems with more than one planet, it is well known that the existence of resonant motion may be possible evidence of a past large-scale planetary migration due to interactions with the gaseous disc. Although their importance is unquestionable, it is still intriguing why some commensurabilities are very populated [e.g. 2/1 mean-motion resonance (MMR)] and others are currently empty (particularly the 1/1 MMR).

Lagrange (1873) discovered stable solutions for three massive bodies such that at all times their relative positions are located in the vertices of an equilateral triangle of variable size (L_4 and L_5 solutions). Linear stability analyses traditionally focused on the restricted three-body problem (where one of the masses vanishes; e.g.

★E-mail: cristian@ua.pt

Namouni, Christou & Murray 1999; Morais 2001 and references therein). Recently, Nauenberg (2002) numerically investigated the dynamical stability of general three-body problem as a function of the eccentricity of the orbits and the Routh mass parameter. The resonant solutions were found stable when $(m_1 + m_2)/\mathrm{M}_\odot \lesssim 0.038$ and up to eccentricities $\sim$0.6. The existence of such periodic orbits in the general three-body problem was also derived, for example, in Siegel & Moser (1971) and Laughlin & Chambers (2002). As mentioned in Laughlin & Chambers (2002), horse-shoe orbits are stable for planetary masses up to $\sim 0.4\,M_{\mathrm{Jup}}$, and despite the first impression, Keplerian fits are good enough to reveal their RV signature with only four orbital periods. We also note that those type of orbits, named 'eccentric resonances', are simply an effect of angular momentum conservation in a coplanar three-body problem, which predicts that when the eccentricity of one planet is maximum the other eccentricity reach a minimum and they have high amplitude of oscillation of resonant angles.

More recently, Hadjidemetriou, Psychoyos & Voyatzis (2009) studied the properties of motion close to a periodic orbit by computing the Poincaré map on a surface of section. They constructed the symmetric families of stable and unstable motion describing one previous unknown symmetric configuration in the general problem, the quasi-satellite (QS) solution.

In a previous work (Giuppone et al. 2010), we studied the stability regions and families of periodic orbits of two planets in the vicinity of a 1/1 MMR, using numerical integrations and developing a semi-analytical method. We considered different ratios of planetary masses and orbital eccentricities, although we assumed that both planets share the same orbital plane (coplanar motion). As a result, we identified two separate regions of stability, symmetric and asymmetric types of motion easily described with the behaviour of resonant angles $(\sigma,\, \Delta\varpi) = (\lambda_2 - \lambda_1,\, \varpi_2 - \varpi_1)$, summarize[1] as follows.

(i) *QS region*. It corresponds to oscillations around a fixed point located at $(\sigma,\, \Delta\varpi) = (0^\circ,\, 180^\circ)$ independent of mass ratio. Although not present for quasi-circular trajectories, they fill a considerable portion of the phase space in the case of moderate to high eccentricities.

(ii) *Lagrangian region*. Two distinct types of asymmetric periodic orbits exist in which both σ and $\Delta\varpi$ oscillate around values different from 0° or 180°. The first is the classical equilateral Lagrange solution associated with local maxima of the averaged Hamiltonian function. Independently of the mass ratio m_2/m_1 and their eccentricities, these solutions are always located at $(\sigma, \Delta\varpi) = (\pm 60^\circ,\, \pm 60^\circ)$. However, the size of the stable domain decreases rapidly for increasing eccentricities, being practically negligible for $e_i > 0.7$.

The second type of asymmetric solutions corresponds to local minimum of the averaged Hamiltonian function. They were named anti-Lagrangian points (AL_4 and AL_5) and, for low eccentricities, are located at $(\sigma,\, \Delta\varpi) = (\pm 60^\circ,\, \mp 120^\circ)$. Each is connected to the classical L_i solution through the σ family of periodic orbits in the averaged system (a family of solutions where the angle σ has zero amplitude of oscillation; e.g. Michtchenko, Beaugé & Ferraz-Mello 2008a,b). Contrary to the classical equilateral Lagrange solution, their location in the plane $(\sigma,\, \Delta\varpi)$ varies with the planetary mass ratio and eccentricities. Although their stability domain also shrinks for increasing values of e_i, they do so at a slower rate than the classical Lagrangian solutions, and are still appreciable for eccentricities as high as $\sim$0.7. An empirical relation exists for eccentricities below 0.6 (e.g. Giuppone et al. 2010; Hadjidemetriou & Voyatzis 2011):

$$e_1 \simeq \left(\frac{m_2}{m_1}\right) e_2. \tag{1}$$

In this paper, we address the question of extrasolar Trojans, both from its detectability and possible origin. In a recent work, Anglada-Escudé, López-Morales & Chambers (2010) showed that two planets in a 2/1 MMR resonance could mimic a single planet in a more eccentric orbit. We wonder whether the opposite could also occur, and if two planets in a co-orbital configuration could give similar RV signals as other dynamical systems including the 2/1 resonance. In Section 2, we review the RV signal generated by such systems and how they can be easily mistaken with the signal generated by a single planet. In the following section, we select representative configurations and generate synthetics data sets for several mass ratio. Section 4 analyses the dynamical stability of the different possible configurations, while the dispersion of the best-fitting parameters is discussed in Section 5. A comparison between two different strategies for planetary detection (two-planet fit versus nested Keplerian fits) is presented in Section 6. Finally, a possible formation mechanism of extrasolar co-orbitals is discussed in Section 7, where we present a series of numerical simulations (both hydro and *N*-body) of two-planet systems immersed in a gaseous disc with an inner gap. Conclusions close the paper in Section 8.

2 KEPLERIAN RADIAL VELOCITY EQUATIONS

First we need to understand some aspects involved in the RV signal produced by two planets in co-orbital motions, assuming unperturbed Keplerian motion. Consider two planets with masses m_1 and m_2 in coplanar orbits around a star with mass $m_0 = \mathrm{M}_\odot$. Let a_i denote the semimajor axes, e_i the eccentricities, λ_i the mean longitudes, ϖ_i the longitudes of pericentre, M_i the mean anomaly and f_i the true anomalies. All orbital elements are assumed astrocentric and osculating.

The suitable angular variables for co-orbital motion are defined by $\sigma = \lambda_2 - \lambda_1$ and $\Delta\varpi = \varpi_2 - \varpi_1$. Disregarding mutual interactions between the planets, the RV of the star is the sum of the individual Keplerian contributions (e.g. Beaugé, Ferraz-Mello & Michtchenko 2007):

$$\begin{aligned} V_r &= K_1[\cos(f_1 + \varpi_1) + e_1 \cos\varpi_1] \\ &\quad + K_2[\cos(f_2 + \varpi_2) + e_2 \cos\varpi_2], \\ &\quad \text{where } K_i = \frac{m_i \sin I_i}{m_i + m_0} \frac{n_i a_i}{\sqrt{1 - e_i^2}}, \end{aligned} \tag{2}$$

I_i being the orbital inclination with respect to the sky. Even though the RV of a star perturbed by the two planets near the periodic orbit (i.e. QS, L_i and AL_i) is not given by a single periodic signal, we may ask under what circumstances this signal could be mimicked by a single planet orbiting the star or even two planets in other configurations.

To address this question, we can use the same approach as that of Anglada-Escude et al. (2010), rearranging the Keplerian contributions from each planet. Using the expansions to first order in

[1] See figs 2 and 5 from Giuppone et al. (2010) in order to easily identify these kind of co-orbital motions in same plane of astrocentric parameters. We centre this work on L_4 and AL_4 configurations since, due to symmetry consideration, they give same results as L_5 and AL_5, respectively.

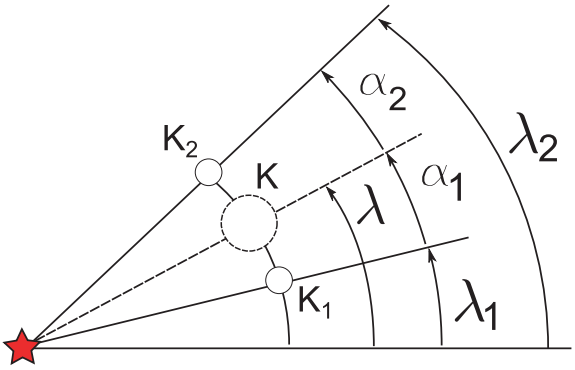

Figure 1. Schematic configuration for co-orbitals and corresponding single planet that mimics their RV signal. The position of single planet is determined by equations (9) and (10).

eccentricities for the true anomaly f (see e.g. Murray & Dermott 1999),

$$\begin{aligned}\sin(f_i) &= \sin(M_i) + e_i \sin(2M_i),\\ \cos(f_i) &= \cos(M_i) + e_i \cos(2M_i) - e_i,\end{aligned} \tag{3}$$

and expanding

$$\cos(f_i + \varpi_i) = \cos(\varpi_i + M_i) + e_i \cos(2M_i + \varpi_i) - e_i \cos\varpi_i, \tag{4}$$

recalling that $\lambda_i = \varpi_i + M_i$ and substituting (4) into (2), we finally obtain

$$\begin{aligned}V_r \simeq\ & K_1[\cos\lambda_1 + e_1\cos(2\lambda_1 - \varpi_1)]\\ & + K_2[\cos\lambda_2 + e_2\cos(2\lambda_2 - \varpi_2)].\end{aligned} \tag{5}$$

Now, we suppose that the previous signal can be mimicked by a single planet. Imagine that its mean longitude λ is located somewhere between the position of co-orbitals. According to Fig. 1, we can rewrite the mean longitudes and the longitudes of pericentres as

$$\begin{aligned}\lambda_1 &= \lambda - \alpha_1,\\ \lambda_2 &= \lambda + \alpha_2, \qquad \text{where} \qquad \alpha_1 + \alpha_2 = \sigma,\\ \varpi_1 &= \varpi - \beta_1,\\ \varpi_2 &= \varpi + \beta_2, \qquad \text{where} \qquad \beta_1 + \beta_2 = \Delta\varpi.\end{aligned} \tag{6}$$

By definition of periodic orbit, $\dot\sigma = 0$ and $\Delta\dot\varpi = 0$, giving constant values for α_1, α_2, β_1 and β_2. We can then substitute equations (6) into equation (5), and regroup terms to rewrite

$$V_r = \underbrace{(K_1\cos\alpha_1 + K_2\cos\alpha_2)}_{\equiv K}[\cos\lambda + e\cos(2\lambda - \varpi)], \tag{7}$$

$$e \equiv \frac{K_1 e_1\cos(2\alpha_1 - \beta_1) + K_2 e_2\cos(2\alpha_2 - \beta_2)}{K_1\cos\alpha_1 + K_2\cos\alpha_2}, \tag{8}$$

where the conditions

$$K_1\sin\alpha_1 = K_2\sin\alpha_2, \tag{9}$$

$$K_1 e_1\sin(2\alpha_1 - \beta_1) = K_2 e_2\sin(2\alpha_2 - \beta_2) \tag{10}$$

eliminate the additional periodic term and also define the position of fictitious single planet, giving

$$\begin{aligned}\tan\alpha_1 &= \frac{K_2}{K_1}\frac{\sin\sigma}{\left(1 + \frac{K_2}{K_1}\cos\sigma\right)},\\ \tan(2\alpha_1 - \beta_1) &= \frac{K_2 e_2}{K_1 e_1}\frac{\sin(2\sigma - \Delta\varpi)}{\left[1 + \frac{K_2 e_2}{K_1 e_1}\cos(2\sigma - \Delta\varpi)\right]}.\end{aligned} \tag{11}$$

It can easily be seen that when both planets have the same mass $\alpha_1 = \alpha_2$ and $\beta_1 = \beta_2$, from which the fictitious single planet would have $\lambda = \frac{\lambda_1+\lambda_2}{2}$ and $\varpi = \frac{\varpi_1+\varpi_2}{2}$. In this case, $e_1 = e_2$ and the RV signal arising from the single planet would be

$$K = 2K_1\cos\frac{\sigma}{2}, \tag{12}$$

$$e = e_1\frac{\cos(\sigma - \frac{\Delta\varpi}{2})}{\cos\frac{\sigma}{2}}. \tag{13}$$

In the opposite limit, when $m_2 \gg m_1$, both α_2, $\beta_2 \to 0$ and the single planet is located near the position of the massive planet. Recall that for co-orbital configuration with eccentricities up to $e_i < 0.6$, the stable zero-amplitude solutions satisfy equation (1), except for the L_4 configuration that always lies in the line segment $e_1 = e_2$.

For other mass ratios, Fig. 2 shows the equilibrium values of α_1, β_1 and the corresponding signal K amplitude and eccentricity e (the eccentricity is shown in units of e_1). Note that the value of e only varies when the single planet mimics co-orbitals in AL_4. It is interesting to remark that QS configuration could easily be mimicked by a single planet of circular orbit.

3 ORBITAL FITS AND SYNTHETIC RADIAL VELOCITY

First we review the differences in radial velocities signals using the Keplerian approximation (2) and N-body integrator, in order to distinguish how important are the mutual interactions and the feasibility of being detected. The top frame of Fig. 3 shows three synthetic

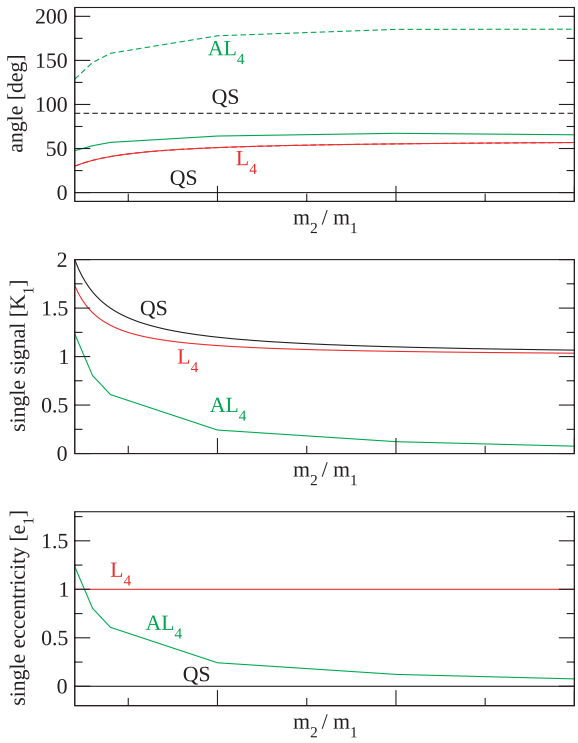

Figure 2. Parameters for a single planet to mimicking the RV signal of two co-orbitals with mass ratio m_2/m_1. The colour code is used to distinguish configurations: QS in black, L_4 in red and AL_4 in green. Top: values of α_1 are shown in continuous lines, while β_1 is plotted in dashed lines. Middle: associated value of K in units of K_1. Bottom: equivalent eccentricity of single planet for each configuration in units of the eccentricity of the co-orbital planet with signal K_1.

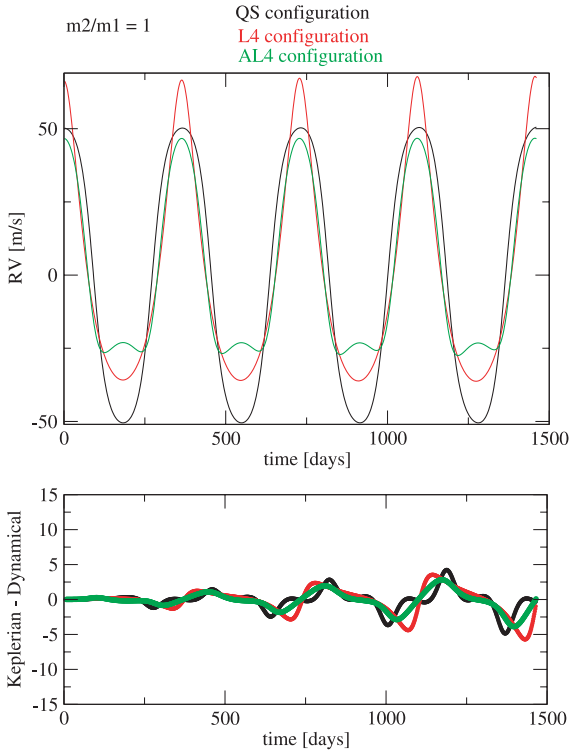

Figure 3. Top: synthetic RV curves generated with an N-body integrator for three different orbital configurations, specified in the top of the graph for the first conditions in Table 1. Bottom: difference between radial velocities calculated from the N-body integration and those generated with Keplerian model. Although the difference increases with time, it remains below 4 m s^{-1} even after four orbital periods.

Table 1. Arbitrary conditions near the stable periodic solutions in the $(\sigma, \Delta\varpi)$ plane, calculated with semi-analytical method. All conditions have $a_1 = a_2$.

	m_2/m_1	σ (°)	$\Delta\varpi$ (°)	e_1	e_2
QS	1	0	180	0.3	0.3
L_4	1	60	60	0.3	0.3
AL_4	1	95.4	257.4	0.3	0.3
QS	3	0	180	0.3	0.1
L_4	3	60	60	0.3	0.3
AL_4	3	77.6	249.7	0.3	0.1

curves covering four orbital periods for equally mass planets ($m_i = M_{\rm Jup}$) in QS, L_4 and AL_4 configurations. The bottom frame of the same figure shows the error that would be obtained if the RV signal was calculated assuming constant Keplerian orbits. Even after four orbital periods, the error remains below $\sim$4 m s^{-1}. As expected, the mutual perturbations would be even smaller if the individual mass were reduced.

To test the mimicking effect described in the previous section, we selected six nominal solutions near exact fixed points chosen from Giuppone et al. (2010), three with $m_1 = m_2$ and the other three with $m_1 = m_2/3$. In all cases, we fixed $m_2 = 1 M_{\rm Jup}$. Initial conditions are summarized in Table 1. In order to test the validity of our expressions (5) and (7)–(8), constructed from a first-order expansion in the eccentricities, here we deliberately chose high eccentric orbits ($e_1 = 0.3$). If our predictions prove correct in these cases, we can be assured that they will be valid for lower eccentricities as well.

For each nominal configuration, we generated a synthetic RV curve describing the stellar motion around the barycentre of the system. The curve was then represented with a discrete sampling of N observation times t_i distributed randomly, according to a homogeneous distribution (thus avoiding aliases in data from daily/seasonal observations; e.g. Dawson & Fabrycky 2010). In each data point, the nominal RV value $V_r(t_i)$ was displaced to a new value $V_{ri} = V_r(t_i) + \mathcal{N}(0, \epsilon)$ following a Gaussian distribution with constant variance ϵ^2. The resulting synthetic data set was then used as input for our orbital fitting code PISA (Pikaia genetic algorithm + simulated annealing; e.g. Beaugé et al. 2008). Since our data sets cover only four orbital periods, the orbital fit was obtained assuming non-interacting Keplerian orbits.

1000 different data sets were generated for each orbital configuration (QS, L_4, AL_4) and each mass ratio m_2/m_1. Each synthetic data set consisted of $N = 100$ data points covering a total of four orbital periods. The results shown here were obtained adopting $\epsilon = 3$ m s^{-1}, a value similar to the present-day errors in detection programs (including stellar jitter). The same analysis was repeated for other values of ϵ, showing similar results although the dispersion around the mean values decreased/increased as a function of (Giuppone et al. 2009).

As noted by Laughlin & Chambers (2002) and Goździewski & Konacki (2006), two planets in a co-orbital configuration produce only one peak in a Fourier spectrum, meaning that it could easily be confused with a single planet (obviously more massive than the individual components). On the other hand, Anglada-Escude et al. (2010) found that two planets in circular orbits near a 2/1 MMR could also be falsely detected as a single planet in an eccentric orbit. So, our question here is the following: is it possible for two planets in different co-orbital configurations (QS, L_4 or AL_4) to be falsely identified as a single planet or as two bodies in a 2/1 resonance?

To test this idea, each of the synthetic data sets was fitted assuming (i) a single planet, (ii) two planets in co-orbital configuration (without specifying the type) and (iii) two planets in the vicinity of a 2/1 MMR. The resulting values of weighted rms ($wrms$) for the 1000 data sets associated with each nominal solution are displayed as histograms in Fig. 4. Each frame corresponds to a given nominal solution and mass ratio, while the colour code for the histograms corresponds to the fitted orbital configurations. For example, in the top left-hand plot we constructed 1000 synthetic data sets from a nominal QS configuration of two planets with equal masses. The data sets were then fitted assuming the three different possible configurations, the resulting values of $wrms$ plotted. The coloured histograms show the distribution of the residuals of each assumed configuration. As we can see, the results corresponding to QS solutions show the smallest distribution of $wrms$ (both in mean and dispersion), very similar to the adopted value of ϵ. Recall that $wrms \sim \epsilon$ is usually employed as evidence that not only the fit is satisfactory but also that the assumed planetary model is correct.

Although for nominal QS solutions and $m_1 = m_2$ the co-orbital configuration gives the best fits, this is not always the case. For systems with a more massive outer body ($m_2/m_1 = 3$), and for any nominal co-orbital motion, we find that all three assumed orbital solutions give practically the same error distribution (right-hand side plots). In other words, it seems that for $m_2 > m_1$ the difference in short-term RV signals of one planet or two bodies in either a 1/1 or 2/1 MMR is virtually indistinguishable. For equal-mass planets, the picture is similar, especially if the nominal configuration corresponds to two planets in L_4. However, two bodies in other co-orbital configurations (i.e. QS or AL_4) appear easier to identify.

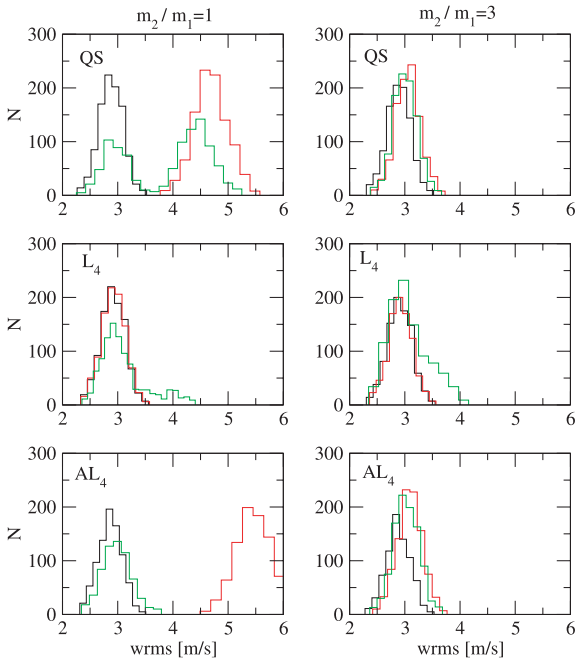

Figure 4. Histograms of residuals adopting different orbital configurations to fit a series of synthetic RV signals. The nominal solution is shown in the top left-hand side of each frame. Each coloured histogram corresponds to a different assumed orbital configuration: two planets in co-orbital motion (black), a single planet (red) and two planets in a 2/1 MMR (green).

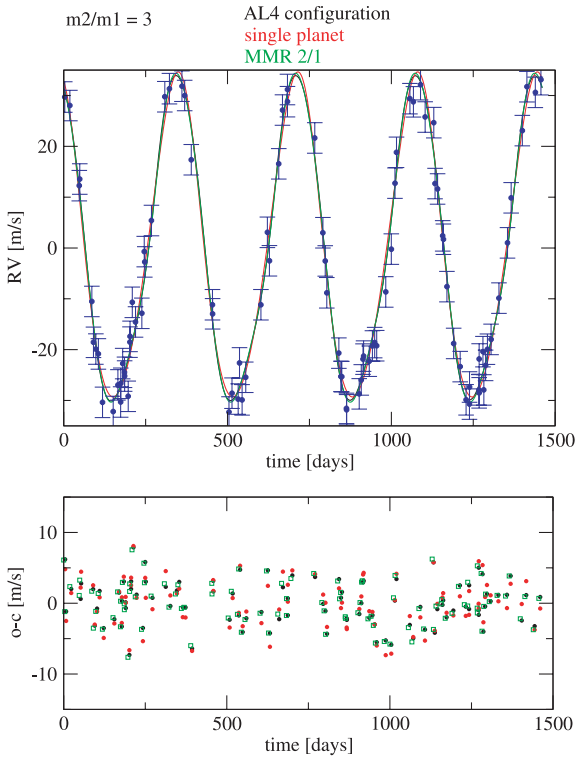

Figure 5. Comparison of synthetic curves (top frame) and residuals (bottom frame) from a nominal AL_4 solution and fitting the synthetic data set with three planetary models: co-orbitals (black), single planet (red) and 2/1 MR (green). The best-fitting values of the masses and orbital elements are shown in Table 2.

Fig. 5 shows an example. The top frame shows a synthetic data set constructed from a nominal solution of two planets in a stable AL_4 configuration. The three different fits are superimposed in different colours and show practically no difference. The corresponding distributions of residuals are shown in the bottom frame, also displaying no significant difference. The best-fitting planetary masses and orbital elements of each orbital configuration are shown in Table 2.

Table 2. Solutions from synthetic data sets generated from configuration AL_4 in Table 1.

Fit model	m_1 ($M_{\rm Jup}$)	m_2 ($M_{\rm Jup}$)	a_1 (au)	a_2 (au)	e_1	e_2	$wrms$ ($\mathrm{m\,s^{-1}}$)
AL_4	0.37	0.9	1	1	0.31	0.127	3.03
One planet	1.12	–	1	–	0.107	–	3.26
2/1 MMR	0.18	1.14	0.63	1	0	0.18	3.05

4 STABILITY ANALYSIS OF THE FITS

Although a given co-orbital pair may be falsely identified as another orbital configuration, we still do not know whether all possible alternatives are equally dynamically stable. To analyse this point, we numerically integrated each of the best fits for a time-span covering 10^4 orbital periods, and calculated the amplitude of oscillation of the resonant angle σ as well as the difference in longitudes of pericentre $\Delta\varpi = \varpi_2 - \varpi_1$. In the case of co-orbital motion, the resonant critical angle is basically the synodic angle $\sigma = \lambda_2 - \lambda_1$, while for the 2/1 MMR we have chosen the so-called principal resonant angle $\sigma = 2\lambda_2 - \lambda_1 - \varpi_1$.

Table 3 presents a statistical analysis of the dynamical evolution of all the best fits. We denote the dynamical behaviour as 'resonant' if the system is stable during the full integration span and both σ and $\Delta\varpi$ show small-to-moderate amplitudes of oscillation ($<50^\circ$) around the fixed point. We call *librators* those configurations where the resonant angle librates but the secular angle circulates. 'Non-resonant' configurations are those for which both angles circulate. Finally, 'unstable' configurations are those that led to collisions or escape of one of the bodies within the integration span.

The left-hand side of Table 3 describes the dynamics of the co-orbital fits. For both mass ratios, the QS solutions appear the most robust. For equal-mass planets, all the fits correctly yield stable resonant QS orbits, fully consistent with the nominal solution. For $m_2/m_1 = 3$, however, 13 per cent of the synthetic data sets led to unstable co-orbital solutions. The reliability of the fits decreases when the adopted nominal solution is L_4 and even worse when it is AL_4. In the latter case, more than a third of the data sets led to unstable solutions.

The right-hand side of the Table 3 now shows results for those fits that incorrectly identified the signal as that generated by two planets in the vicinity of the 2/1 MMR. For equal-mass planets, the best fits are highly unstable for both QS and L_4 nominal configurations, while the AL_4 data give a 63 per cent of stable configurations but with both resonant angles circulating. When we increase the mass ratio, the compatible 2/1 MMR solutions are slightly more stable although again correspond mainly to non-resonant configurations. Again, the QS and L_4 configurations are the most unfavourable for being labelled as 2/1 MMR solutions, although for asymmetric equilateral Lagrange solutions a small fraction (∼8 per cent) of 2/1 MMR solutions show stable librators.

Table 3. Percentage of different dynamical outcomes of the best fits for different mass ratios m_2/m_1. The value of m_2 was fixed at $1M_{\rm Jup}$. See text for a detailed description.

	m_2/m_1	Co-orbital fit		2/1 MMR fit			
		Resonant (per cent)	Unstable (per cent)	Resonant (per cent)	Librators (per cent)	Non-resonant (per cent)	Unstable (per cent)
QS	1	100	0	0	0	2	98
L_4	1	98	2	0	7	3	92
AL_4	1	84	13	0	0	63	37
QS	3	83	13	0	3	16	81
L_4	3	81	18	0	6	7	87
AL_4	3	62	38	0	8	31	61

5 DISPERSION OF THE BEST-FITTING PARAMETERS

Although the best fits assuming two planets in a 2/1 MMR have proved to be largely unstable, and thus difficult to confuse with co-orbital planets, we have no clear indication of the cause of the instability. In this section, we will analyse the planetary masses and eccentricities obtained form the diverse best fits, and compare them with the nominal solutions.

Results are presented in Figs 6–8 for equal-mass planets ($m_1 = m_2 = M_{\rm Jup}$). Each corresponds to a different nominal co-orbital solution (QS, L_4 and AL_4, respectively), and is divided into four frames. The top graphs show histograms with the distribution of the eccentricities (left) and deduced planetary masses (right). Masses

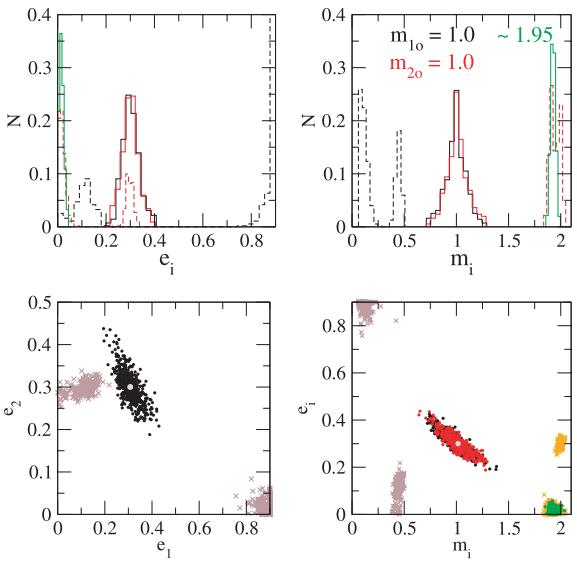

Figure 6. Dispersion of best-fitting solutions from synthetic data sets for two planets with $m_1 = m_2 = M_{\rm Jup}$ in a QS solution. Top: distribution of the best-fitting eccentricities (left) and planetary masses (right). The single-planet fit is shown in a continuous green line. For the two-planet fits, the results for planet 1 are shown in black, while those corresponding to planet 2 are shown in red. In these cases, continuous lines are used for the co-orbital configuration, while dashed lines correspond to a 2/1 MMR fit. Bottom left: scatter plot showing the dispersion of best-fitting eccentricities. Results for the co-orbital fit are shown in black, while those corresponding to a 2/1 MM fit are shown in grey. Bottom right: scatter plot with the dispersion of eccentricity as a function of planetary mass. Black and red dots correspond to both planets of a co-orbital solution, orange and grey correspond to the planets of a 2/1 MMR and green points are the single-planet solutions. Grey circles were drawn to identify nominal configurations.

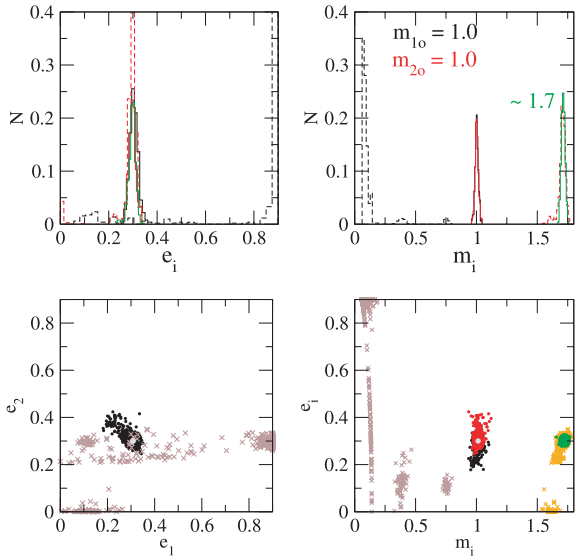

Figure 7. Same as Fig. 6, but for two planets with $m_1 = m_2$ in an L_4 configuration.

are in units of $M_{\rm Jup}$. Different colours and line types correspond to different configuration or bodies (see caption for details). The two bottom plots show the dispersion of the eccentricities (left) and relation between the mass and eccentricities (right). Once again, different colours are used for different configurations/bodies.

For a nominal QS configuration (Fig. 6), the best-fitting parameters assuming a co-orbital solution show a considerable dispersion: approximately 0.04 in eccentricities and $0.1M_{\rm Jup}$ in masses. However, there appears to be no appreciable systematic error, and both distributions seem symmetric with respect to the nominal values. The single-planet fits show a very steep distribution around $e \simeq 0$ and $m \simeq 2$. To understand this result, we can analyse the expected RV signal. For a QS configuration, we have $\sigma = 0^\circ$ and $\Delta\varpi = 180^\circ$. Moreover, from equation (1) we have that equal-mass planets imply $e_1 = e_2$, from which we expect $K_1 = K_2$. Consequently, equation (7) leads to

$$V_r = 2K_1 \cos\lambda. \tag{14}$$

This tells us that two planets in QS orbit produce the same signal as one planet with semi-amplitude $K = 2K_1$ and eccentricity $e = 0$. The dispersion of the best fits shows an excellent agreement with this prediction, yielding a planet with $m = m_1 + m_2$ in a quasi-circular orbit. Surprisingly, the dispersion of the different fits is smaller than that obtained assuming (correct) QS orbits.

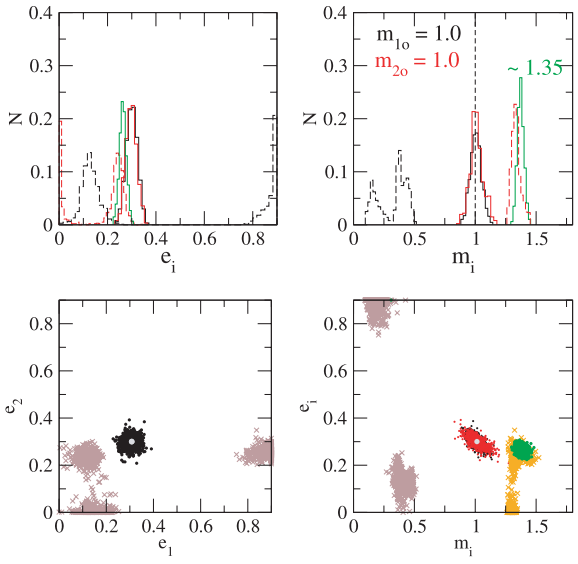

Figure 8. Histograms of fitted synthetic data sets for two equally mass planet in AL_4 configuration.

The distribution of the 2/1 MMR fits, shown in the histograms with dashed lines, shows a strong bimodal shape. Approximately half of the best fits give masses in the vicinity of $(m_1, m_2) \sim (2, 0.5)$ and eccentricities around $(e_1, e_2) \sim (0, 0.3)$. The other half of the solutions clutter around $(m_1, m_2) \sim (2, 0.1)$ and $(e_1, e_2) \sim (0.1, 0.8)$. This indicates the existence of two local minima in the residual function with similar values of the *wrms* and similar extension in the parameter space. Small differences in the synthetic data sets would then highlight one or the other, thereby yielding either two planets in low-to-moderate eccentricities or a solution in which one of them is almost parabolic. However, as shown in Table 3, practically all solutions are unstable.

Results for a nominal L_4 configuration are shown in Fig. 7. Contrary to the previous case, the co-orbital fits now show a very narrow dispersion around the correct solution, implying that the RV signal of two planets in an equilateral configuration is more robust than two bodies in QS. Applying equation (7) to this case yields $\alpha_1 = \alpha_2 = 30^\circ$, and the same RV signal could also be associated with a single planet with

$$V_r = \sqrt{3} K_1 [\cos\lambda + e\cos(2\lambda - \varpi)], \quad (15)$$

where $e = e_1 = e_2$ is the value of the eccentricity of the original bodies. The distribution of the best single-planet fits follows this prediction and shows a very sharp peak at $(m, e) = (\sim 1.7, 0.3)$.

The 2/1 MMR best fits always give two planets with a large mass ratio. The largest body has mass and orbital elements similar to the single-planet fit, while its companion has very small mass and very high eccentricity ($K \to \sigma$ and $e \to 1$). Thus, this second planet does little more than attempt to resolve the residuals of the single-planet solution. It is therefore no surprise that practically all resonant configurations are highly unstable.

Finally, Fig. 8 shows the results obtained from a nominal AL_4 configuration. Initial conditions show a small amplitude oscillation around the equilibrium solution $(\sigma, \Delta\varpi) = (95.^\circ 4, 257.^\circ 46)$ which, substituting into equation (7), leads to an equivalent single-planet solution with

$$V_r = 1.34 K_1 [\cos\lambda + 1.24\, e_1 \cos(2\lambda - \varpi)], \quad (16)$$

which results in the strong peak in the mass and eccentricity histograms. However, all one-planet solutions have much larger residuals than the co-orbital solution (see Fig. 4). Once again, the solutions assuming a 2/1 MMR generate a bimodal distribution, with part of the solutions (∼33 per cent) with high eccentricities and consequently unstable. However, contrary to the previous cases, almost two-thirds of the fits lead to configurations that are dynamically stable, even if the resonant angles are in circulation. These correspond to $m_1 \sim 0.4$ and $e_1 < 0.2$.

The same procedure was also followed for synthetic data sets with $m_2/m_1 = 3$ and $e_2 = e_1/3$. Results showed very similar traits as those presented for equal-mass planets, except for a larger dispersion in the parameters. This larger dispersion diminishes the proportion of stable co-orbital fits (see Table 3) but also allows for a significant number of stable fits assuming two planets in a 2/1 MMR. In the case of a nominal AL_4 configuration, almost one-third of the synthetic data sets gave stable 2/1 configurations, although only a fraction of these corresponded to libration.

6 NESTED VERSUS TWO-PLANET FITS

Apart from possible misidentification of co-orbital planets as other configurations, the 1:1 MMR also appears sensitive to the strategy adopted for the fitting algorithm. There are two commonly used procedures to fit a two-planet solution into a given RV data set. One possibility, the *simultaneous two-planet fit*, assumes the existence of two masses from the beginning, and attempts to fit the data set with a model with two periodic signals. The second approach, sometimes referred to as the *nested model*, first attempts to fit one planet into the data. If the residuals are too large or if its Fourier spectrum shows a significant periodicity, then a second planet is fitted into the reduced data. Typically, this is adopted if the largest amplitude of the spectrum is larger than a given false alarm probability (FAP).

In a perfect world, both procedures should give the same results, or at least very similar to each other. This appears to be the case for non-resonant planets or even for planets in the 2/1 MMR (see the analysis done by Beaugé et al. 2008, for the HD 82943 system). However, as we will show below, they can lead to completely different solutions in the case of co-orbital planets.

Using the same type of nominal configurations shown before, we generated new synthetic RV data sets. We incorporated two differences: first, the orbital period of the planets was raised to 400 d. Secondly, the data covered 12 years (10 complete periods) with $N = 200$ randomly distributed observations assuming $\epsilon = 5\,\mathrm{m\,s^{-1}}$. We repeated the same test fits as in the previous section with similar results.

We now use the same data to compare both fitting strategies. Results are shown in Fig. 9. All the periodograms were calculated using data-compensated discrete Fourier transform (DCDFT; Ferraz-Mello 1981) which allows a treatment of unequally spaced data. In the top and middle frames, the power spectra are normalized so that the total area is unity. The top graph shows the periodogram of the original data, where the main 400 d signal is clearly visible. The middle frame shows the power spectra of the residuals after a single-planet fit. The dashed horizontal line corresponds to an FAP of 10^{-4}, and was estimated using the Quast algorithm (Ferraz-Mello & Quast 1987). We note the existence of peak corresponding to a period near $P = \frac{1}{3} P_1$ which appears statistically relevant. After performing a second planet fit, the *wrms* was reduced from 6.6 to $5.6\,\mathrm{m\,s^{-1}}$.

Finally, the lower frame shows periodograms of the residuals after both two-planet fits. Black curves show the results employing a nested model, while the red curve corresponds to a simultaneous

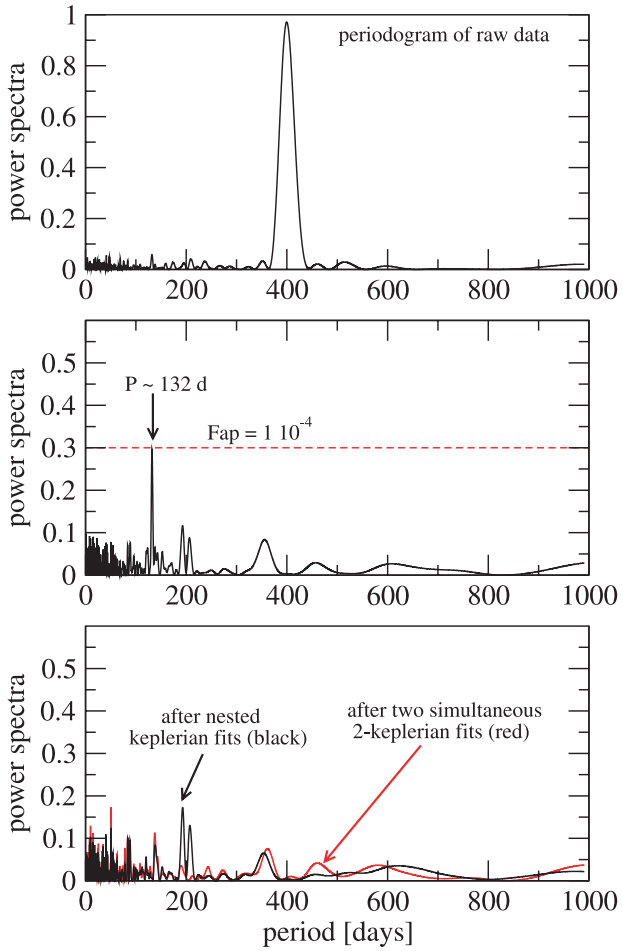

Figure 9. Top: power spectra of a synthetic data of two co-orbital planets with orbital period of 400 d. Middle: power spectra of the residuals after a single-planet fit. Horizontal dashed line marks the 99.99 per cent confidence level. Bottom: power spectra obtained from the residuals of two different two-planet fits. Red corresponds to a simultaneous fit of two massive bodies, while the black curve is the results of a nested two-planet model.

two-planet model. The power spectra are quite similar and no additional periodicity is observed. The resulting masses and planetary parameters of both models are given in Table 4. Although both results are very different, not only are the *wrms* very similar, but also the incorrect system derived from the nested model is dynamically stable. In fact, the orbital eccentricities derived from the nested model are actually significantly lower than the nominal values. Finally, we found no appreciable difference by using *N*-body fits for this data set.

The top frame of Fig. 10 shows, in blue, the data synthetic points of the fictitious QS configuration. The black curve presents the expected RV signal from a nested two-planet fit, while the red curve corresponds to a simultaneous fit of both planets. The bottom plot gives the resulting O − C, showing practically no difference between both fits.

7 ORIGIN OF EXOTROJANS

In the first part of this paper, we have analysed whether a co-orbital configuration could give RV signals similar to other dynamical systems, which may explain why so far no co-orbitals have been discovered. In this second part, we focus on a possible formation mechanism.

Table 4. Best multi-Keplerian orbital fits for the data generated by two equal-mass planets in a QS co-orbital configuration. The time of passage through the pericentre τ is given with respect to the time of the first data point. All orbital elements are astrocentric and osculating.

	Simultaneous two-planet fit		Nested two-planet fit	
Parameter	Planet 1	Planet 2	Planet 1	Planet 2
K (m s^{-1})	28.59	31.00	54.19	5.26
P (d)	396.9	402.2	399.62	132.25
e	0.3421	0.2696	0.0194	0.1835
m ($M_{\rm Jup}$)	1.8757	1.8469	1.96	0.13
a (au)	0.7461	1.1779	1.06	0.508
V_0 (m s^{-1})	−0.051		0.05	
$wrms$ (m s^{-1})	5.004		5.62	
$\sqrt{\chi^2_\nu}$	1.027		1.154	

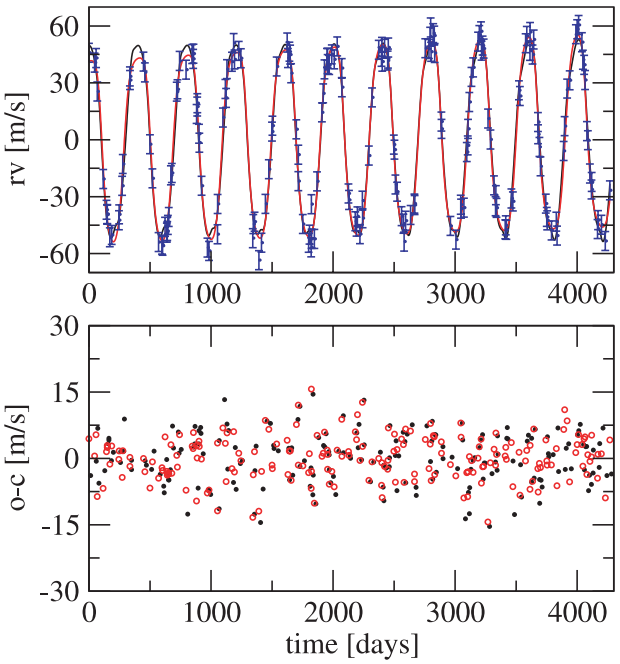

Figure 10. Top: synthetic data set of observations (marked as blue dots) and two curves generated with solutions obtained with co-orbital simultaneous fit (red) and two nested single fits (black). Bottom: residuals from both fits showing no significant differences.

There is a vast literature trying to explain the formation of Trojan planets. Several different mechanisms have been proposed, including accretion from protoplanetary disc (Laughlin & Chambers 2002), pull-down capture into the 1/1 resonance, direct collisional emplacement, and in situ accretion (Chiang & Lithwick 2005), or convergent migration of multiple protoplanets (Thommes 2005; Cresswell & Nelson 2006).

Kortenkamp (2005) studied the gravitational scattering of planetesimals by a protoplanet, revealing that a significant fraction of scattered planetesimals (between 5 and 20 per cent) can become trapped as QS in heliocentric 1/1 co-orbital resonance with the protoplanet. They included a solar nebula gas drag and considered planetesimals with diameters ranging from ∼1 to ∼1000 km. The initial protoplanet eccentricities were chosen from $e = 0$ to 0.15 and protoplanet masses range from 300 down to 0.1 $M_\oplus$.

A different possibility was analysed by Cresswell & Nelson (2006), where the authors used a hydrodynamical code to simulate the evolution of systems of up to 10 planets with masses between 2 and 20 $M_\oplus$. After a brief period of chaotic interaction characterized by scattering, orbital exchanges and collisions, some cases led to co-orbital planets occupying either horse-shoe or tadpole orbits. If the initial separation between bodies was taken $\Delta \sim 5R_{\rm Hill}$, such configurations occurred in 20 per cent of the runs, while the probability increased to 80 per cent if the initial separation was reduced to $\Delta = 4R_{\rm Hill}$. They also found that planets sometimes evolved from horse-shoe to tadpole configurations, although some co-orbital configurations were short-lived, ultimately leading to disruption and escape of one of its members.

Beaugé et al. (2007) studied the in situ formation of terrestrial-like Trojan planets starting from a swarm of planetesimals initially located around the Lagrangian point L_4 of a massive planet. They analysed different masses, initial conditions and both gas-free and gas-rich scenarios. The swarm of prototrojans were initially located within the L_4 tadpole region with total masses ranging from 1 to 3 $M_\oplus$. The gas interaction was modelled using linear and non-linear gas drags in an N-body code, adjusting the parameters to reproduce preliminary tests done with the FARGO hydrodynamical code. Their main results showed that the accretional process within the co-orbital region is not very efficient, and the mass of the final Trojan planet never seems to exceed 0.6 $M_\oplus$.

Hadjidemetriou & Voyatzis (2011) studied the evolution of a QS system under the additional effects of a gas drag. They found that a QS planetary system with initially large eccentricities can migrate along the family of periodic orbits and be finally trapped in a satellite-type orbit. Thus, the authors provided a mechanism for the generation of satellite systems starting from a planetary configuration. These results agreed with those obtained numerically by Kortenkamp (2005).

Morbidelli et al. (2008) complete this brief picture, analysing the interactions between several planetary cores and a 'density jump' in a gaseous disc. Depending on the planetary masses and initial conditions, they found cases of resonance trapping, scattering and even the formation of temporary binaries.

In this paper, we follow the same scenario of Morbidelli et al. (2008) to analyse whether co-orbital systems may also be formed through the interaction of two planets with a density jump in protoplanetary disc. We thus consider two planets initially far from mean-motion commensurabilities that migrate inwards, ultimately becoming locked in resonance. We assume that the disc possesses an inner cavity which acts as a planetary trap, halting the migration of the massive bodies. For simplicity, we consider a constant surface density $\Sigma_{\rm o}$ outside the cavity, and a constant value $\Sigma_{\rm i}$ inside. The density jump is set at a radial distance $r = 1$ (arbitrary units) from the star. Thus, we characterize the density jump in the disc by two main parameters: the density ratio $F = \Sigma_{\rm o}/\Sigma_{\rm i}$ and the width Δ of the cavity edge (see Fig. 11).

Our main simulations were performed using the FARGO-2D public hydrocode, whose basic algorithm may be found in Masset (2000). This code solves the Navier–Stokes equations for a Keplerian disc subject to the gravity of the central object and that of embedded planets. The disc is assumed isothermal and not self-gravitating.

7.1 Preliminary N-body simulations

Before undertaking the main hydrosimulations, we wish to analyse what disc properties ($\Sigma_{\rm o}$, F, Δ, etc.) and planetary parameters (masses, initial separation, etc.) are compatible with the formation of co-orbital solutions. Since such a broad sweeping of the parameter space is extremely time consuming for a hydrocode, we employed an N-body code for a series of preliminary runs. The interaction between the planets and the disc was approximated by a type I migration following the semi-analytical model of Tanaka, Takeuchi & Ward (2002) and Tanaka & Ward (2004). In the case of a smooth density profile, explicit expressions for the forces acting on the planetary masses can be found in Ogihara, Duncan & Ida (2010).

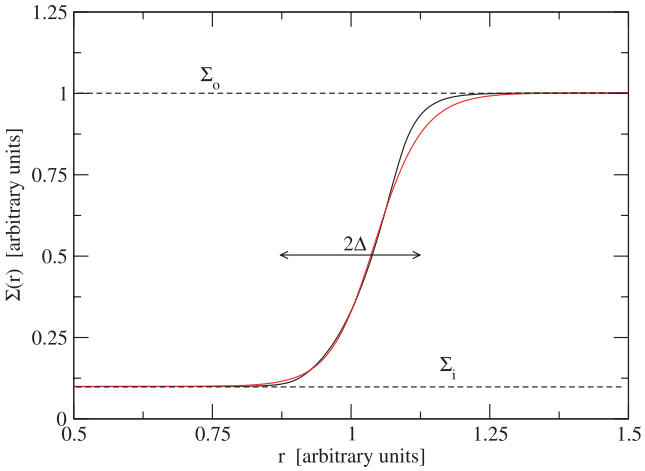

Figure 11. Surface density of the gas disc in the vicinity of a density jump or inner cavity. $\Sigma_{\rm o}$ and $\Sigma_{\rm i}$ are the values outside and inside the jump, also characterized by a half-width Δ. The black curve shows the azimuthal average $\Sigma(r)$ obtained from a hydrodynamical simulation (FARGO), while the red curve is the analytical approximation using equation (17).

Since we will be working with planetary masses smaller than $1M_{\rm Sat}$, type I migration is expected to be a fair description of the tidal interactions with the disc. However, we stress that these N-body simulations are not expected to be accurate, but are used solely as guidelines for the full hydrosimulations introduced in the following sections.

The inner cavity in the disc may be approximated with a hyperbolic tangent, such that

$$\ln \Sigma(r) = C_a \tanh x + C_b, \quad \text{with} \quad x = \frac{r-1}{\Delta}, \tag{17}$$

and where the coefficients are given by

$$C_a = \frac{1}{2}(\ln \Sigma_{\rm o} - \ln \Sigma_{\rm i}), \quad C_b = \frac{1}{2}(\ln \Sigma_{\rm o} + \ln \Sigma_{\rm i}). \tag{18}$$

Fig. 11 shows two representations of $\Sigma(r)$ with a test cavity (edge at $r = 1$). The black curve was generated with FARGO (see Benítez-Llambay, Masset & Beaugé 2011, for details), while the red curve was obtained applying equation (17). Both appear very similar, although the analytical function has a smoother trend near the edges of the cavity.

Having an explicit functional form for the density profile, we can modify Tanaka's equations for the corotational torque to reproduce the contribution generated by a density jump in the disc. This was done following the calculations deduced in Masset et al. (2006a), and the resulting expressions were incorporated into our N-body code. With this tool we were then able to reproduce the dynamical behaviour of massive planets near the density jump without needing to artificially halt the planet at a given orbital distance from the star.

Benítez-Llambay et al. (2011) showed that the real population of close-in exoplanets is consistent with a disc inner cavity located at

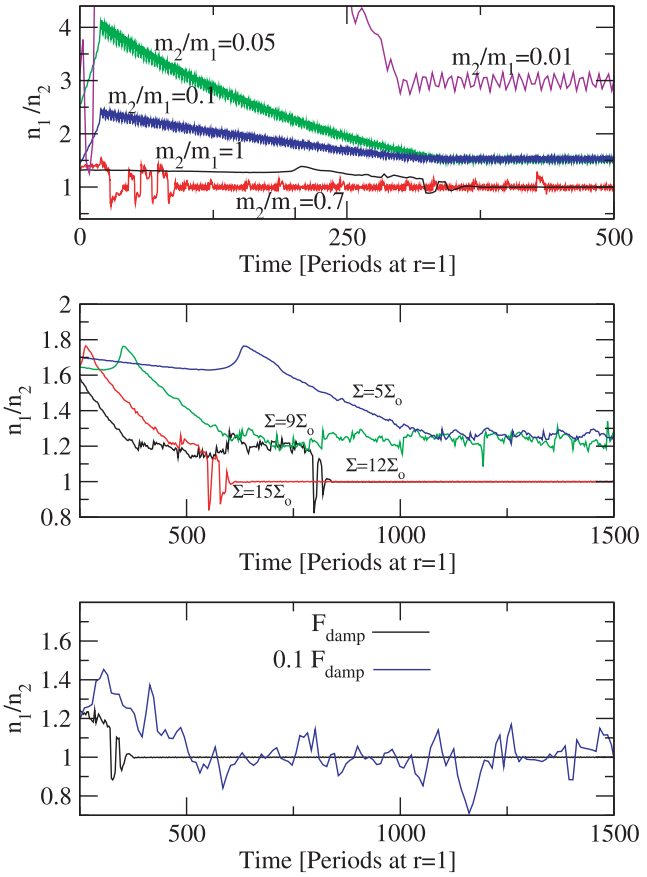

Figure 12. *N*-body simulations of two planets encountering an inner cavity in the disc located at $r = r_0 = 1$ (arbitrary units). Top: using constant value for density ($\Sigma_o = 15\Sigma_o$) and different pairs of planets with mass ratio from 10^{-2} to 1. The co-orbital configuration is achieved if the mass ratio is $0.7 < m_2/m_1 < 1.4$, this range becoming wider for increasing values of Σ_o. Middle frame: two Saturn-mass planets in a disc with different Σ_o. For values larger than $12\Sigma_o$, final co-orbital configurations appear with high probability. Bottom frame: two simulations with $m_1 = m_2 = M_{Sat}$ and $\Sigma_o = 15\Sigma_o$, but considering different magnitudes for the eccentricity damping. Meanwhile, planet 1 was fixed at 1.5 au, we change the position of planet 2 from 1.9 to 3.2 au in order to represent better the results in the figure.

$r_0 \sim 0.01$ au. However, since our *N*-body simulations will be used primarily as a stepping stone into hydrosimulations, it is preferable to scale the initial conditions to $r_0 = 1$. Appendix A shows the scale transformations necessary for the gas density and time units to ensure the same dynamics. For example, assuming a typical surface density for the disc of $\Sigma \sim 5800\,\mathrm{g\,cm^{-2}}$ at $r = 1$ au, the corresponding value at any arbitrary spatial scaling parameter r_0 gives $\Sigma = 6.4 \times 10^{-4}\,\mathrm{M_\odot}\, r_0^{-2}$, where r_0 is given in au.

Fig. 12 shows the results of several simulations using our modified *N*-body code with a density jump centred at $r = r_0 = 1$ and with a half-width of $\Delta = 2H/r$. Throughout all our simulations, both *N*-body and hydro, we assumed a disc scaleheight equal to $H/r = 0.05$ and a depth of the cavity equal to $F = \Sigma_o/\Sigma_i = 10$. The density outside the cavity will be set to $\Sigma_o = N\Sigma_o$, with N a positive integer and $\Sigma_o = 10^{-3}\,\mathrm{M_\odot\,au^{-2}}$. In other words, we will perform simulations with different surface densities given as multiples of an arbitrary base value Σ_o.

All plots show the time evolution of the ratio of mean motions n_1/n_2 between both planets. In the top plot, we considered a fixed value of $\Sigma_o = 15\Sigma_o$, but varied the mass ratio of the bodies in the interval $m_2/m_1 \in [10^{-2}, 10^0]$. In all cases, the mass of the largest body was equal to $1M_{Sat}$.

Since m_1 has the smallest initial semimajor axis, as well as the largest mass, its orbit suffers a faster orbital decay, and is the first planet to reach the cavity edge. In all the runs, this body was trapped near the centre of the density jump ($r \sim 1.05r_0$) with a small eccentricity. Meanwhile, the outer approaches the cavity edge, encountering successive and increasingly strong MMRs in its path. The orbital evolution is then dictated by two opposing forces: (i) the differential disc torque that subtracts angular momentum and causes further orbital decay and (ii) resonant perturbations with the inner mass that can generate conditions for a net increase in the angular momentum.

The top plot of Fig. 12 shows that the system is stopped at different MMRs depending on the mass ratio. For small values of m_2/m_1, the two planets are trapped in the 3/1 MMR, while the 3/2 commensurability is favoured for larger mass ratios. This is expected, since a larger outer mass requires stronger resonance perturbations to counteract the disc torque. For $m_2/m_1 \geq 0.7$, however, it appears no commensurability is sufficiently strong, and both bodies reach the cavity edge and evolve towards a stable co-orbital configuration.

From these results it then appears that co-orbital planets may be formed at a density jump in the disc if the mass ratio is sufficiently close to unity. We checked that the same result was obtained for other mass values, considering planets ranging from Neptune to Jupiter analogues.

The middle plot of Fig. 12 now analyses the dependence on the value of the surface density Σ_o outside the cavity, while maintaining the same cavity depth F. Results are shown for two equal-mass planets ($m_1 = m_2 = M_{Sat}$) and four different multiples of the base density Σ_o. We note that smaller densities favour resonance trapping in non-co-orbital configurations (e.g. 5/4 MMR), but for large values of Σ_o, typically above $\Sigma_1 \sim 10\Sigma_o$, co-orbital systems are the usual outcome. Of course, there is some dependence on the initial conditions, mainly on the initial separation of the bodies, but these results are surprisingly robust and are representative of most of our runs.

Finally, the bottom frame shows the dependence on the eccentricity damping force F_{damp}. Although both the circularization timescale τ_e and the orbital decay time τ_a have the same dependence with the planetary mass and disc density (e.g. Tanaka & Ward 2004), it is possible to fictitiously modify the eccentricity damping by changing the tangential force suffered by the bodies. Our main aim in this experiment is to see how the dynamics may be affected by different values of τ_e/τ_a. The plot shows two simulations, one with the correct value of τ_e (black) and the other in which the damping rate was reduced by a factor of 10 (blue). Although a co-orbital configuration was achieved in both cases, the reduced damping generates a much larger amplitude of oscillation of the eccentricities which may ultimately lead to orbital instability. In fact, some of these simulations showed complex exchanges between different types of co-orbital solutions (L_4, L_5, etc.).

In conclusion, our preliminary *N*-body simulations appear to indicate that co-orbital systems of massive planets can be obtained if the mass ratio is sufficiently close to unity and the surface density of the disc is sufficiently high. Although the final outcomes have a certain dependence on the initial conditions (like all resonance trapping phenomena), we repeated the runs for initial separations between 0.5 and $1.7r_0$, finding no significant changes in the results. Inspired by these results, our next step is to upgrade to hydrodynamical simulations.

7.2 Hydronumerical set-up

Our hydrosimulations were carried out using the FARGO code (Masset 2000) with a central star of $1\,M_\odot$. We consider two-dimensional, locally isothermal discs uniformly distributed over a polar grid.

The disc inner cavity was generated using an ad hoc step in kinematic viscosity around $r = r_0 = 1$, using the same recipe as described in Masset et al. (2006a). For all our runs, we adopted a cavity depth of $F = \Sigma_o/\Sigma_i = 10$, and a half-width of $\Delta = 0.4$. The kinematic viscosity was considered uniform outside the cavity, and equal to $\nu = 10^{-5}\, r_0^2\, \Omega_0^{-1}$, where Ω_0 is the orbital frequency at radius r_0. The disc aspect ratio was chosen as $H/r = 0.05$ and also constant over r. Boundary conditions were chosen to be non-reflecting for the inner edge of the disc.

The disc was represented with a spatial resolution of 384 azimuthal zones and 168 radial zones. The inner radius of the disc is set to $0.42r_0$ and the outer radius is set to $4.2r_0$. This resolution allows us to identify details as small as $0.04r_0$. Casoli & Masset (2009) showed that the co-orbital corotation torque exerted by the disc over a planet occurs in a scale of $x_s \sim 0.01 r_0$ for $m \sim 2\,M_\oplus$, while Masset, D'Angelo & Kley (2006b) showed that the horse-shoe zone width in a two-dimensional disc scales as $x_s = 1.16\sqrt{q/h}$. Consequently, x_s should increase with the planetary mass. For example, if we are interested in the dynamical evolution of Saturn-type planets, we expect that our choice for the spatial resolution should be adequate.

To test this idea, we performed several simulations with the same initial conditions but different spatial resolutions for the disc, and compared the dynamical evolution of the planets. An example is shown in Fig. 13 for two Saturn-like planets initially in circular orbits far from the cavity edge and in non-resonant conditions. Both simulations show the same qualitative results, not only in the final outcome of the planets (both runs end in co-orbital configurations) but also in the behaviour of the eccentricities. The only notable change is a slight difference in the radial distance at which the planets are trapped. However, this is not significant and could be explained due to a decrease of the corotational torque from a low-resolution description of the horse-shoe region.

Following the predictions of our N-body runs, all our hydrosimulations were done with two equal-mass planets ($m_1 = m_2$) in a high-density disc. Initial conditions were varied with respect to both the initial separation between the planets and the initial eccentricities. We also considered different planetary masses between $1\,M_\oplus$ and $1 M_{\rm Sat}$.

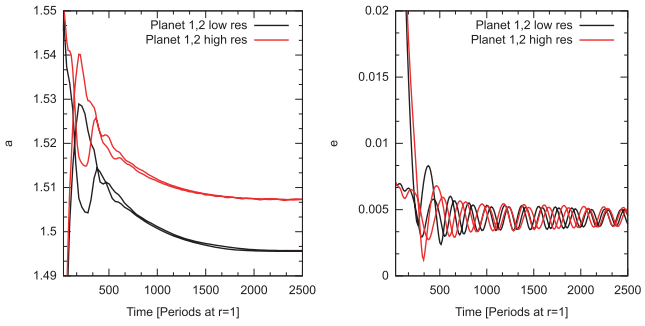

Figure 13. Comparison between two hydrosimulations with the same initial conditions (see text for details) but different grid resolutions. The high-resolution simulation was constructed with 306 radial zones, while the low-resolution run contained only 168 radial zones. Both lead to co-orbital configurations with similar global dynamical features.

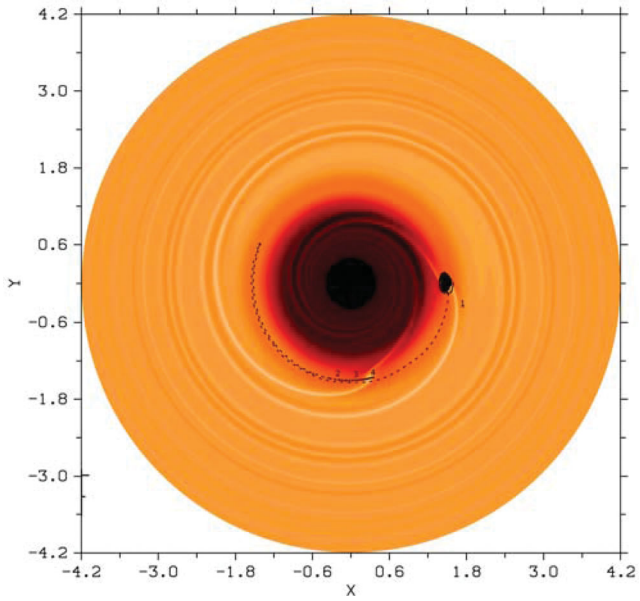

Figure 14. Snapshot of the final outcome of a high-resolution (306 radial zones) hydrosimulation leading to two planets locked in a co-orbital configuration. One of the planets (m_1) is fixed in the x-axis. The numbers 1, 2, 3 and 4 represent the location of the other planet (m_2) at different times of the run, with number 4 being the final configuration.

Under a wide variety of initial conditions, we found that the orbital evolution of two Saturn-mass planets ultimately leads to the formation of stable co-orbital configurations. An example is shown in Fig. 14, where both bodies are trapped in L_4/L_5-type motion with a libration of both the resonant angle $\sigma = \lambda_2 - \lambda_1$ and the difference in longitudes of pericentre $\Delta\varpi = \varpi_2 - \varpi_1$.

To test the robustness and stability of the co-orbital solutions to additional perturbations, we performed a new series of runs including additional six Earth-mass planets initially far from the cavity edge. The idea behind this set of experiments is to analyse both the orbital evolution of these new bodies as well as their effects on the two co-orbitals. Typical results are shown in Fig. 15, where each colour curve corresponds to a different planet (see inlaid colour code). Planets 1 and 2 (i.e. m_1 and m_2, respectively) are the original Saturn-mass bodies in co-orbital motion, while planets 3–8 are the new Earth-size masses. Since this type of simulation included smaller masses and a larger population, we employed a high-resolution description of the disc.

We perceived no significant instability in the co-orbitals, and their configuration remained unaffected by the new masses. These, however, suffered several cases of mutual scattering and close encounters that caused the ejection of three of the masses. One of the close encounters (between planets 4 and 6) led to a temporary trapping of planet 4 in the cavity edge but finally led to the formation of a new co-orbital system with planet 8. The role of scattering between planets as a formation mechanism for co-orbitals has already been pointed out by Cresswell & Nelson (2006). The final outcome of this system consists of an inner co-orbital system, a single Earth-mass planet trapped in an exterior MMR and an additional co-orbital pair in another resonance. Although this appears a very complex multiple resonant configuration, we found no indication of long-term instability.

Fig. 16 shows the dynamics of both pairs of co-orbitals: planets 1 and 2 are displayed on the left-hand plots, while the co-orbital system composed of planets 4 and 8 is shown on the right. Top

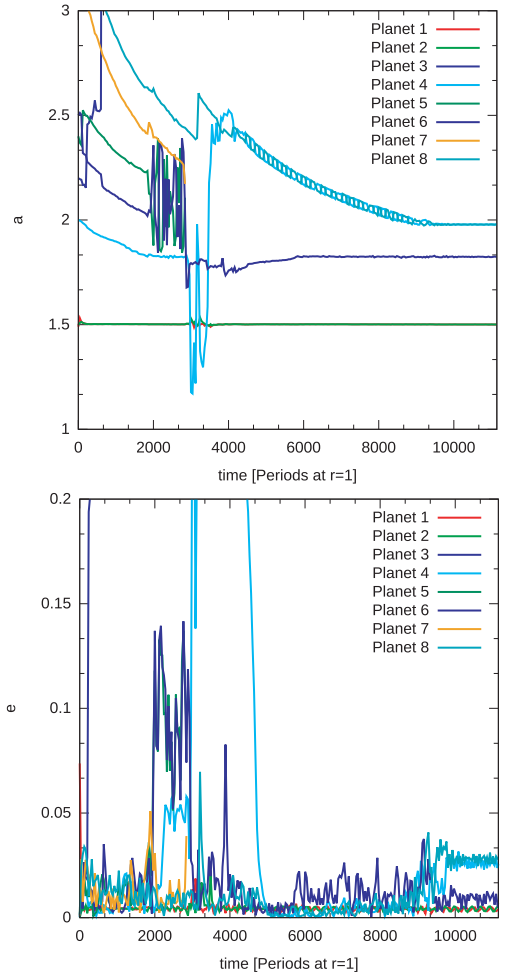

Figure 15. Results of a low-resolution (168 radial zones) hydrosimulation of eight planets with masses in the Earth–Saturn range. Top plot shows the semimajor axis as a function of time, while the lower frame shows the eccentricities.

graphs present the temporal evolution of the resonant angle $\sigma = \Delta\lambda = \lambda_2 - \lambda_1$, while the middle plots show $\Delta\varpi = \varpi_2 - \varpi_1$. Once planet 4 is scattered into the cavity, the resonance relation between planets 1 and 2 is temporarily disrupted, resulting in a short-lived circulation of both angles. However, once the Earth-mass planet is sent back outside the cavity, the co-orbital configuration of the inner planets is re-established, although around L_5 instead of L_4. We did some follow-up integrations without hydrodynamical interaction choosing two intermediate stages as initial conditions. The bottom left-hand plot shows the results of choosing as initial conditions the system configuration at $t = 450$ and 11 450, respectively. The behaviours of both critical angles show a small amplitude libration around the equilibrium solutions. Between these two solutions, the system experiments temporarily AL_4 and AL_5 configurations.

The dynamical evolution of the small-mass pair is more complex, and a stable configuration is only reached near the end of the simulation, and corresponds to an AL_5-type orbit with large amplitude of oscillation of $\Delta\varpi$ or about 150°.

8 CONCLUSIONS

In this paper, we have analysed the detectability and possible formation mechanism of hypothetical massive planets in stable co-orbital

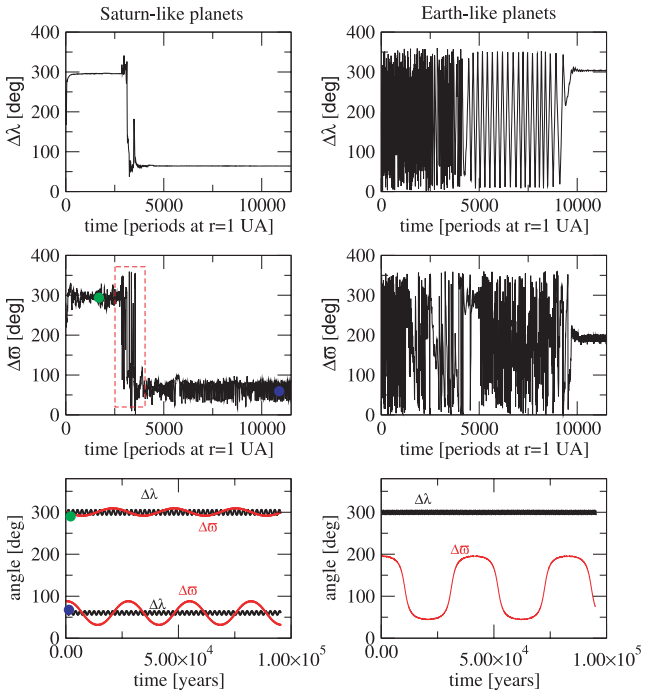

Figure 16. Evolution of characteristics angles for co-orbital solutions (top frame $\Delta\lambda$ and middle frame $\Delta\varpi$) during the hydrosimulation. We reserve left-hand side to the system 1–2 and right-hand side to the system 4–6. We plot in the lower frames the evolution of characteristics angles integrating the system without considering the interaction with the disc. At left frame, two conditions were chosen, one at $t = 450$ and the other at $t = 11450$ (marked as colour circles in the middle frame), meanwhile at right bottom frame the final configuration of Earth-like planets was integrated.

configurations. So far, there are no known extrasolar planetary systems containing co-orbital bodies, which may imply that these configurations are extremely difficult either to form or to detect from RV surveys.

We have studied the detectability of three different types of co-orbital motion (QS, L_4/L_5 and AL_4/AL_5), trying to evaluate possible bias in detections and identify what kind of compatible configuration could be detected. The analysis of Keplerian contributions to radial velocities allowed us to predict the value for the signal of one single planet that could be confused with co-orbital configurations.

For even low values of errors in radial velocities measurements ($\epsilon = 3\,\mathrm{m\,s^{-1}}$) and observation time-spans covering four orbital periods (which include most of the presently detected exoplanets), co-orbital configurations appear hard to identify: the results of the fitting process could easily confuse the RV data with that stemming from other configurations/systems (single planet or 2/1 MMR system). For large mass ratios, a correct identification of co-orbital configuration is even more complicated and easier to confuse with the other configurations. In all cases, the residuals of the different systems are comparable, even more so for large mass ratios (see Fig 4).

Observation data sets covering longer time-spans allow us to detect mutual perturbations, but once again the best fits are not always associated with co-orbital motion. We have found several cases where other resonant configurations (i.e. 3/1 commensurability) actually give smaller residuals and better results.

Co-orbital motion is sensitive not only to the data set, but also to the fitting procedure. Nested two-planet strategies may also confuse the real dynamics and yield results widely different from the

nominal orbits; in this sense, simultaneous two-planet fits seem more robust.

Transit observations should help distinguish co-orbitals planets from other solutions.

Finally, we have found that stable co-orbital systems with two massive planets may be formed from originally non-resonant orbits through their interaction with an inner cavity in the protoplanetary disc, as long as the surface density of the disc is sufficiently large. Both our *N*-body and hydrosimulations indicate a preference towards co-orbitals with similar masses (i.e. $m_1 \sim m_2$). In all our simulations with large mass ratios, the smaller planet was either pushed inside the cavity or trapped in a mean-motion commensurability outside the density jump.

ACKNOWLEDGMENTS

This work has been supported by the Argentinian Research Council – CONICET – and the Fundação para a Ciência e a Tecnologia (FCT) of Portugal.

REFERENCES

Anglada Escudé G., López-Morales M., Chambers J. E., 2010, ApJ, 709, 168
Beaugé C., Ferraz-Mello S., Michtchenko T. A., 2007, in Dvorak R., ed., Extrasolar Planets: Formation, Detection and Dynamics. Wiley-VCH, Weinheim
Beaugé C., Giuppone C. A., Ferraz-Mello S., Michtchenko T. A., 2008, MNRAS, 385, 2151
Benítez-Llambay P., Masset F., Beaugé C., 2011, A&A, 528, A2
Casoli J., Masset F., 2009, ApJ, 703, 845
Chiang E. I., Lithwick Y., 2005, ApJ, 628, 520
Cresswell P., Nelson R. P., 2006, A&A, 450, 833
Dawson R., Fabrycky D. C., 2010, ApJ, 722, 937
Ferraz-Mello S., 1981, AJ, 86, 619
Ferraz-Mello S., Quast G., 1987, in Kleczek J., ed., Exercises in Astronomy. D. Reidel, Dordrecht, p. 231
Giuppone C. A., Tadeu dos Santos M., Beaugé C., Ferraz-Mello S., Michtchenko T. A., 2009, ApJ, 699, 1321
Giuppone C. A., Beaug C., Michtchenko T. A., Ferraz-Mello S., 2010, MNRAS, 407, 390
Goździewski K., Konacki M., 2006, ApJ, 647, 573
Hadjidemetriou J., Voyatzis G., 2011, Celest. Mech. Dynamical Astron., 111, 179
Hadjidemetriou J., Psychoyos D., Voyatzis G., 2009, Celest. Mech. Dynamical Astron., 104, 23
Kortenkamp S., 2005, Icarus, 175, 409
Lagrange J. L., 1873, in Serret J.-A., ed., Oeuvres de Lagrange, Vol. 6. Gauthier-Villars, Paris, p. 272
Laughlin G., Chambers J. E., 2002, AJ, 124, 592
Masset F., 2000, A&AS, 141, 165
Masset F. S., Morbidelli A., Crida A., Ferreira J., 2006a, ApJ, 642, 478
Masset F. S., D'Angelo G., Kley W., 2006b, ApJ, 652, 730
Michtchenko T. A., Beaugé C., Ferraz-Mello S., 2008a, MNRAS, 387, 747
Michtchenko T. A., Beaugé C., Ferraz-Mello S., 2008b, MNRAS, 391, 227
Morais M. H. M., 2001, A&A, 369, 677
Morbidelli A., Crida A., Masset F., Nelson R. P., 2008, A&A 478, 929
Murray C. D., Dermott S. F., 1999, Solar System Dynamics. Cambridge Univ. Press, Cambridge
Namouni F., Christou A. A., Murray C. D., 1999, Phys. Rev. Lett., 83, 2506
Nauenberg M., 2002, AJ, 124, 2332
Ogihara M., Duncan M. J., Ida S., 2010, ApJ, 721, 1184
Siegel C. L., Moser J. K., 1971, Lectures on Celestial Mechanics. Springer-Verlag, Berlin
Tanaka H., Ward W. R., 2004, ApJ, 602, 388
Tanaka H., Takeuchi T., Ward W. R., 2002, ApJ, 565, 1257
Thommes E. W., 2005, ApJ, 626, 1033

APPENDIX A: ABOUT THE SCALE OF SIMULATIONS

All our simulations were performed with a density jump centred at $r_0 = 1$. If we wish to relate our results to another scale, for example $r_0 = 0.01$, we need to modify not only the spatial scale of the orbital system but also the surface density value. Here, we present a simple recipe for the scale transformations in order to preserve the complete dynamics, including both the gravitational interactions and migration time-scale.

The equation of motion of a planet with mass m_i interacting gravitationally with other N bodies of mass m_j is given by

$$\frac{\mathrm{d}^2 \boldsymbol{r}_i}{\mathrm{d}t^2} = -\sum_{j \neq i} \frac{G m_j}{r_{ij}^2} \boldsymbol{e}_{ij}, \tag{A1}$$

where $\boldsymbol{e}_{ij}$ are the unit vectors corresponding to the relative positions. If we introduce a scale change in the coordinates defined by $r = \alpha r'$ and a temporal transformation defined by $t = \beta t'$, then the gravitational dynamics is invariant if $\beta = \alpha^{3/2}$.

In our problem, however, the dynamical evolution of the planets also includes their interaction with the gas disc, which is specified by the gradient of the total differential torque Γ. If we then desire to preserve the complete dynamics of the system under the spatial rescaling, then the torque must scale as

$$\Gamma = \alpha^{-1} \Gamma'. \tag{A2}$$

For a type I migration, the total torque is given by $\Gamma(r) \propto \Sigma(r) n^2 r^4$, where n is the mean motion. We also assume that the surface density is given by a power-law expression of the type

$$\Sigma(r) = \Sigma_\mathrm{o} \left(\frac{r}{r_0} \right)^\eta, \tag{A3}$$

for a suitable exponent η. The coefficient Σ_o denotes the surface density at $r = r_0$. Then, if we apply the spatial and temporal transformations required to preserve the gravitational dynamics, we obtain

$$\Gamma = \alpha \Sigma_\mathrm{o} \left(\frac{r'}{r'_0} \right)^\eta n'^2 r'^4 = \alpha \left(\frac{\Sigma_\mathrm{o}}{\Sigma'_o} \right) \Gamma'. \tag{A4}$$

Therefore, for scaling our simulation to a new suitable value of r_0, it is necessary to do the transformation

$$r = \alpha r', \tag{A5}$$

$$t = \alpha^{3/2} t', \tag{A6}$$

$$\Sigma_\mathrm{o} = \alpha^{-2} \Sigma'_\mathrm{o}. \tag{A7}$$

For this new radius, time and density value, the dynamics of system is invariant.

This paper has been typeset from a TEX/LATEX file prepared by the author.